HOKKAIDO UNIVERSITY

Title	Initiation and propagation of small fatigue crack in beta titanium alloy observed through synchrotron radiation multiscale computed tomography
Author(s)	Xue, Gaoge; Nakamura, Takashi; Fujimura, Nao; Takahashi, Kosuke; Oguma, Hiroyuki; Takeuchi, Akihisa; Uesugi, Masayuki; Uesugi, Kentaro
Citation	Engineering Fracture Mechanics, 263, 108308 https://doi.org/10.1016/j.engfracmech.2022.108308
Issue Date	2022-03-15
Doc URL	http://hdl.handle.net/2115/91130
Rights	© 2022. This manuscript version is made available under the CC-BY-NC-ND 4.0 license
Rights(URL)	http://creativecommons.org/licenses/by-nc-nd/4.0/
Type	article (author version)
File Information	Revised manuscript-clean_final_20220205.pdf

Instructions for use

Hokkaido University Collection of Scholarly and Academic Papers : HUSCAP

Initiation and propagation of small fatigue crack in beta titanium alloy observed through synchrotron radiation multiscale computed tomography

Gaoge Xue[a], Takashi Nakamura[b,*], Nao Fujimura[b], Kosuke Takahashi[b], Hiroyuki Oguma[c], Akihisa Takeuchi[d], Masayuki Uesugi[d], and Kentaro Uesugi[d]

[a]*Division of Mechanical and Space Engineering, Hokkaido University, Japan*
[b]*Division of Mechanical and Aerospace Engineering, Hokkaido University, Japan*
[c]*Research Center for Structural Materials, National Institute for Materials Science, Japan*
[d]*Japan Synchrotron Radiation Research Institute (JASRI), SPring-8, Japan*

*Corresponding author: nakamut@eng.hokudai.ac.jp

ABSTRACT:

Synchrotron radiation computed tomography is an emerging nondestructive method for fracture analysis in materials. Herein, the *in situ* small-crack growth of a beta titanium alloy, Ti–22V–4Al, was monitored by a combination of microtomography (micro-CT) and nanotomography (nano-CT). The 3D characteristics of small cracks and the corresponding stress intensity factor range (ΔK) were obtained by micro-CT; the cracks initiated at ~10% fatigue life. In the low-ΔK regime, the scatter of the crack aspect ratio and the deviation in the crack propagation rate were significant; however, they decreased with increasing ΔK, reflecting the microstructural effect on small-crack propagation. The microstructure of the beta titanium alloy was successfully visualized by nano-CT. Consequently, the crack–surrounding-microstructure interactions evidenced that the fatigue cracks initiated from the center of the beta grain wherein the alpha-phase was less precipitated.

Keywords: Non-destructive inspection; crack initiation; small-crack growth; beta titanium; nanotomography

1. Introduction

Beta titanium alloys have been attracting much attention as promising structural materials owing to their excellent mechanical properties and corrosion resistance. While they have been increasingly employed in the aerospace industry [1–3], research on their fatigue behavior has gained considerable importance in the recent past [4–11]. The fatigue crack in beta titanium alloys is mostly initiated at a crystallographic level, which belongs to a small-crack regime rather than a large-crack regime. The difference between the small- and large-crack behaviors has been thoroughly investigated, which has led to a consensus that they cannot be treated equally. Small cracks exhibit a considerably higher propagation rate during the early stage than large cracks, and they are more vulnerable to microstructural factors [12–15]. These results indicate that small-crack growth experiments are crucial for accurately estimating their behaviors in the initial stage of fatigue fractures.

However, conventional small-crack growth experiments suffer from several significant shortcomings. Because small cracks were analyzed only on the basis of the specimen surface, little information was obtained regarding the internal structure of the specimen. For instance, the investigation of the crack-shape evolution during the growth, which can be critical for determining the crack intensity, is unclear and challenging. In addition, because of the small order of the initiated crack size (approximately 10 μm), observing the mutual interactions between the crack and its surrounding microstructure is difficult, particularly in the direction of depth. To overcome these shortcomings in small-crack growth experiments, a nondestructive inspection technique with a high spatial resolution is required.

Synchrotron radiation X-ray computed tomography (SR-CT) has recently emerged as a novel method for fatal-defect detection [16–18] and direct investigation of the failure process [19–29]. Projection-type X-ray microtomography (micro-CT) is a widely used SR-CT technique. This technique can provide a spatial resolution in the order of micrometers and a field of view (FOV) in the order of millimeters, which facilitate the batch detection of naturally initiated small cracks. However, the

micrometer-order spatial resolution is inadequate to investigate the crack and microstructural effects at an early stage with only a few grains. High-energy phase-contrast X-ray nanotomography (nano-CT) has been recently proposed and has attracted much attention [30,31]. While conventional nano-CT requires an extremely small sample with a size in the order of hair thickness to allow sufficient X-ray penetration, high-energy nano-CT enables a sample size up to the millimeter order; thus, nondestructive inspection can be conducted while meeting industrial standards. In this study, the applied nano-CT has a spatial resolution of approximately 100 nm, which allows for an in-depth analysis of microstructural factors and their visualization to a great extent. However, the narrow FOV of nano-CT poses a challenge in locating the initiated crack. Therefore, micro-CT and nano-CT must be employed synthetically to understand the relationship between the local microstructure and behaviors of small-crack growth. In our previous nano-CT studies, we observed the crack and its surrounding microstructure in an alpha + beta titanium alloy Ti–6Al–4V [30]. However, nano-CT imaging of beta titanium alloys is still a challenge because the high density of beta stabilizer elements (e.g., vanadium and manganese) reduces the X-ray transmittance to a greater extent than titanium and alpha stabilizer elements (e.g., aluminum) do. In other words, satisfying the optimized conditions for nano-CT imaging in beta titanium alloys is highly challenging.

Herein, we applied the beamline BL20XU at SPring-8, a third-generation synchrotron radiation facility located in Hyogo, Japan [32]; it provides both micro-CT and nano-CT, which can be toggled freely, called multiscale tomography [33]. An *in situ* small-crack growth test of a beta titanium alloy was conducted on the beamline. Micro-CT was used to detect the initiated crack and its propagation behavior. Nano-CT was subsequently applied to investigate the mutual interactions between the initiated crack and its surrounding microstructure.

2. Materials and Methods

2.1 Material and specimen

The experimental material was a commercial metastable titanium alloy, Ti–22V–4Al, (Material code DAT51) developed by Daido Steel Co., Ltd., Japan [34]; its chemical composition includes 4.15% Al, 21.17% V, 0.15% Fe, 0.14% O, 0.013% C, and 0.0124% H. The as-received material was a Φ18 mm × 250 mm round bar. The heat-treatment process was as follows: a solution treatment at 1023 K for 1 h followed by water quenching and then aging at 823 K for 4 h followed by air cooling. Here, the heating rates of solution treatment and aging were greater than 2000 K/h and 1000 K/h, respectively. The microstructure and mechanical properties of the heat-treated material are presented in Fig. 1 and Table 1, respectively. The alpha phase precipitates unevenly from the grain boundary, leading to a microstructure with a beta-phase residual in the center of the grain and an acicular alpha phase near the grain boundary. The average grain size is 20 μm.

To obtain adequate X-ray transmittance, the specimen diameter should be sufficiently small. In this study, the control volume of the specimen was first lathe-turned to a diameter of 0.8 mm with a length of 3 mm, as shown in Fig. 2. To remove the hardened layer due to the lathe-turning process, the control volume was sequentially polished using #800–#2000 emery papers to achieve a diameter of 0.7 mm.

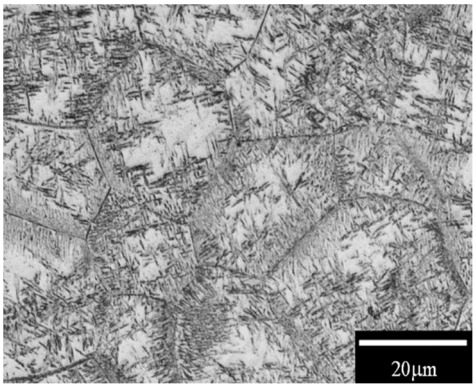

Fig. 1 SEM image of the microstructure of the heat-treated Ti–22V–4Al alloy with coarse, acicular alpha-phase precipitation.

Table 1 Mechanical properties of the heat-treated alloy, Ti–22V–4Al.

0.2% Proof Stress [MPa]	**Tensile Strength [MPa]**	**Elongation [%]**	**Reduction of Area [%]**
850	967	21.9	58.2

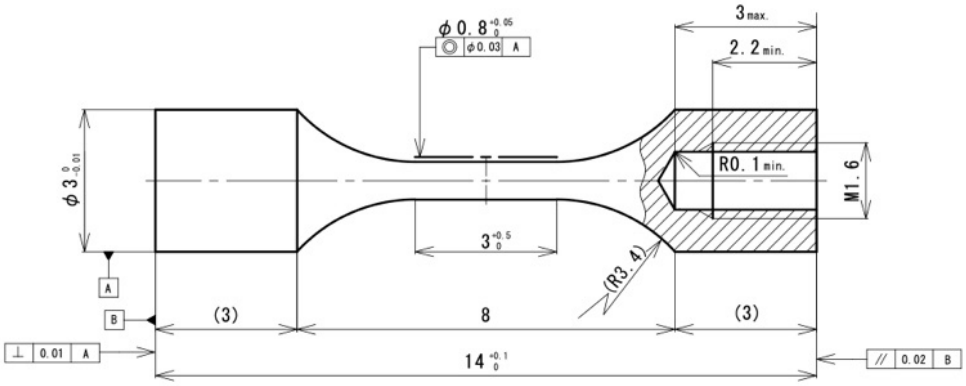

Fig. 2 Configuration of the specimen (units: mm).

2.2 Instrumentation of fatigue testing setup

An *in situ* piezo fatigue-testing machine was developed to perform fatigue tests on the beamline, as illustrated in Fig. 3. The employed piezo actuator was PSt 150/10/200 VS15 (Piezomechanik Co., Ltd). The working range of the voltage was from −30 V to 150 V, providing a maximum stroke of 270 μm. The capacities of the tensile and compressive loads were 600 N and 3800 N, respectively. During the imaging process, the entire system was set on a rotation stage. According to Fig. 3, X-rays originate from the left direction, pass through the PMMA (polymethyl methacrylate) cylinder and the specimen, and finally enter the image detector. In addition, to avoid overheating of the piezo actuator, an air coolant was introduced through the air inlet. A digital servo controller (Shimadzu 4830) was applied to generate a waveform and to control the fatigue test.

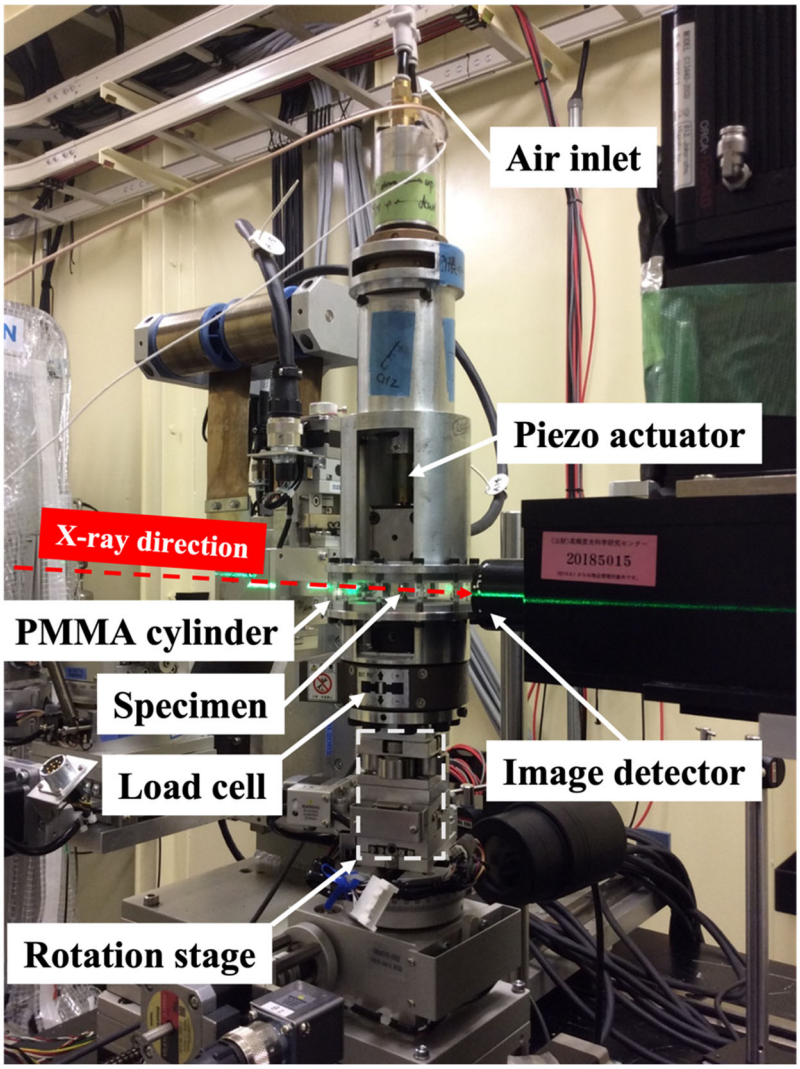

Fig. 3 *In situ* piezo fatigue-testing setup.

2.3 Imaging conditions

The beamline BL20XU at SPring-8 includes two experimental hutches, which are separated from each other by 160 m. The sample (the specimen installed in the *in situ* fatigue-testing machine) was set up in the first hutch. The imaging mode can be switched between micro-CT and nano-CT without moving the sample. In the micro-CT mode, the X-rays directly pass through the sample and are detected by the image detector located at the first hutch. Upon switching to the nano-CT mode, a condenser zone plate and a pinhole are induced, and the imaging detector in the first hutch is removed by stepping motors. Accordingly, the X-rays pass through an apodization Fresnel zone plate and a Zernike phase plate and are finally captured by the image detector at the second hutch. Additional details on the employed CT system can be

referred to in the literature [30,33]. For both the employed imaging modes, the sample was rotated about the longitudinal axis from 0° to 180° with a step of 0.1° during the imaging process, which provided 1800 radiographs per scan. The imaging conditions of micro-CT and nano-CT were determined by individual experiments. The details are listed in Table 2. The conditions of nano-CT were optimized for microstructural visualization, as discussed in Section 4.1.

Table 2 Imaging conditions of micro-CT and nano-CT.

Imaging mode	Micro-CT	Nano-CT
X-ray energy (keV)	30	
Binning mode	1 × 1	
Exposure time (ms)	25	4000
Voxel size (μm)	0.5	0.0387
Sample–detector distance (m)	0.06	~160
Field of view (mm × mm)	1 × 1	0.063 × 0.063
Total scan duration (min)	~10	~120

2.4 Testing procedure

The fatigue properties of the experimental material are demonstrated in Fig. 4 [35]. Owing to the limit of beamline operation time, the test condition was determined as the maximum stress of 650 MPa, which was 76% of the proof stress under a stress ratio $R = -1$ to reach a relatively short fatigue life. The corresponding fatigue life was approximately 10^4 cycles. For the *in situ* small-crack growth test, the experimental steps were as follows. First, a micro-CT image was captured prior to the fatigue test. The fatigue test and CT imaging were then repeated. The intervals of the loading cycles (ΔN) and CT mode were determined for each purpose. To capture the small-crack initiation, micro-CT was conducted with a ΔN of 500 cycles until 2000 cycles. Micro-CT images were obtained at 0, 500, 1000, 1500, and 2000 loading cycles. Subsequently, nano-CT was performed on the initiated crack for additional local microstructural details. After 2000 cycles, CT imaging was conducted with a ΔN of 1000 cycles to clearly observe the crack-propagation behavior until the specimen was fractured. The testing frequency was set at 10 Hz. To open the crack, a tensile load equivalent to 50% of the maximum stress was applied to the specimen during CT imaging.

The obtained CT images were analyzed using ImageJ software [36]. A schematic of a crack with relevant parameters is shown in Fig. 5. The horizontal crack length at the specimen surface, $2a$ (hereinafter called "crack length"), and crack depth, b, were specifically focused in this study.

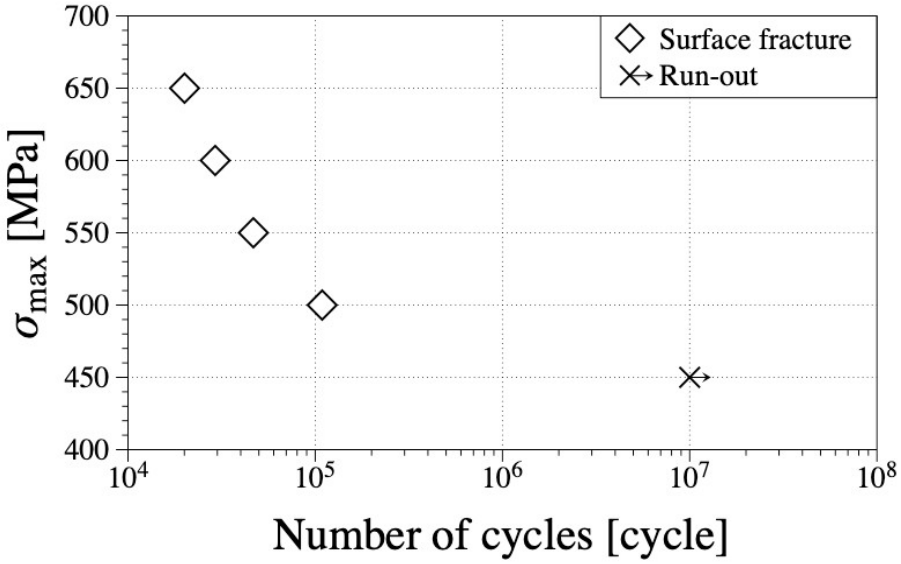

Fig. 4 Fatigue properties of the experimental material under a stress ratio, $R = -1$.

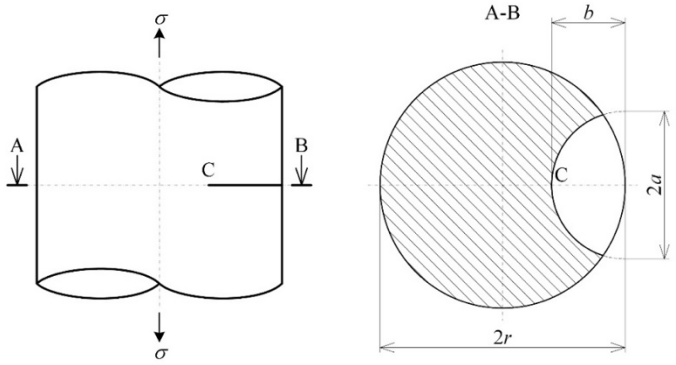

Fig. 5 Schematic of the crack and relevant parameters.

3. Micro-CT results

3.1 Crack-initiation status

During the tests, multiple small cracks were initiated at the specimen surface. The crack initiation location on a plane perpendicular to the loading axis as well as the crack-initiation life (N_i) and crack-initiation length ($2a_{ini}$) are illustrated in Fig. 6 (a).

The side view of the specimen as well as the images of the cracks initiated on the virtual cross section parallel to the longitudinal direction are demonstrated in Fig. 6 (b). In this study, N_i and $2a_{ini}$ of each crack were defined as the number of cycles and the crack length upon crack detection, respectively.

As described in Section 2.4, micro-CT imaging was conducted at 0, 500, 1000, 1500, and 2000 cycles to detect the initiated cracks. The first four cracks are detected at 1000 cycles, which is approximately 10% of the average fatigue life. These four cracks, labeled counterclockwise from C-1 to C-4, were randomly distributed on the specimen surface. In addition, another crack, C-5, which was initiated at 1500 cycles, was detected at the same location as that of C-1 in the XY plane but a different Z axis. The average $2a_{ini}$ of the five cracks was 9.3 μm, which was much smaller than the average grain size (20 μm), implying that crack initiation was successfully captured. In the present study, these five cracks were chosen for the further investigation of the crack-growth behaviors.

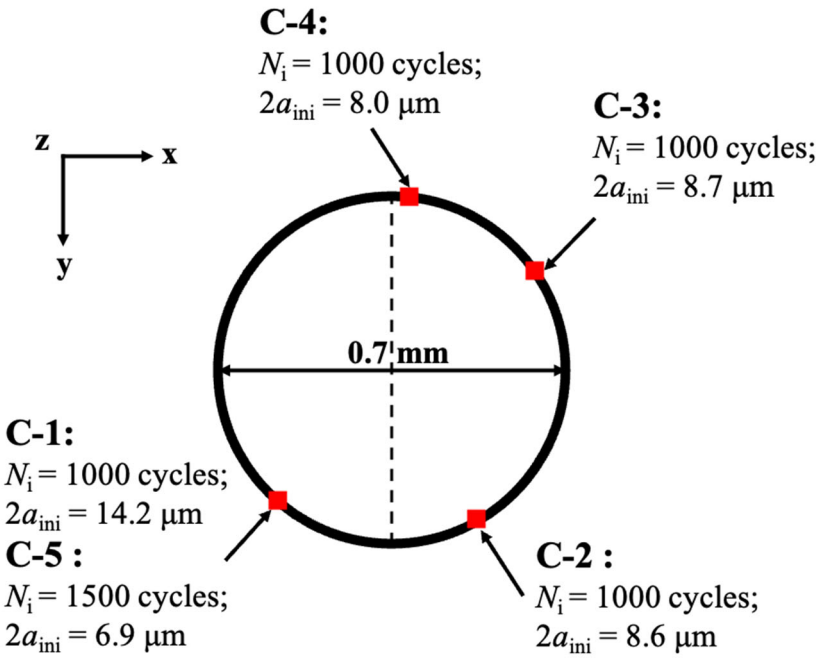

(a) Crack-initiation location on the plane perpendicular to the loading axis, with the corresponding initiation life and crack length values

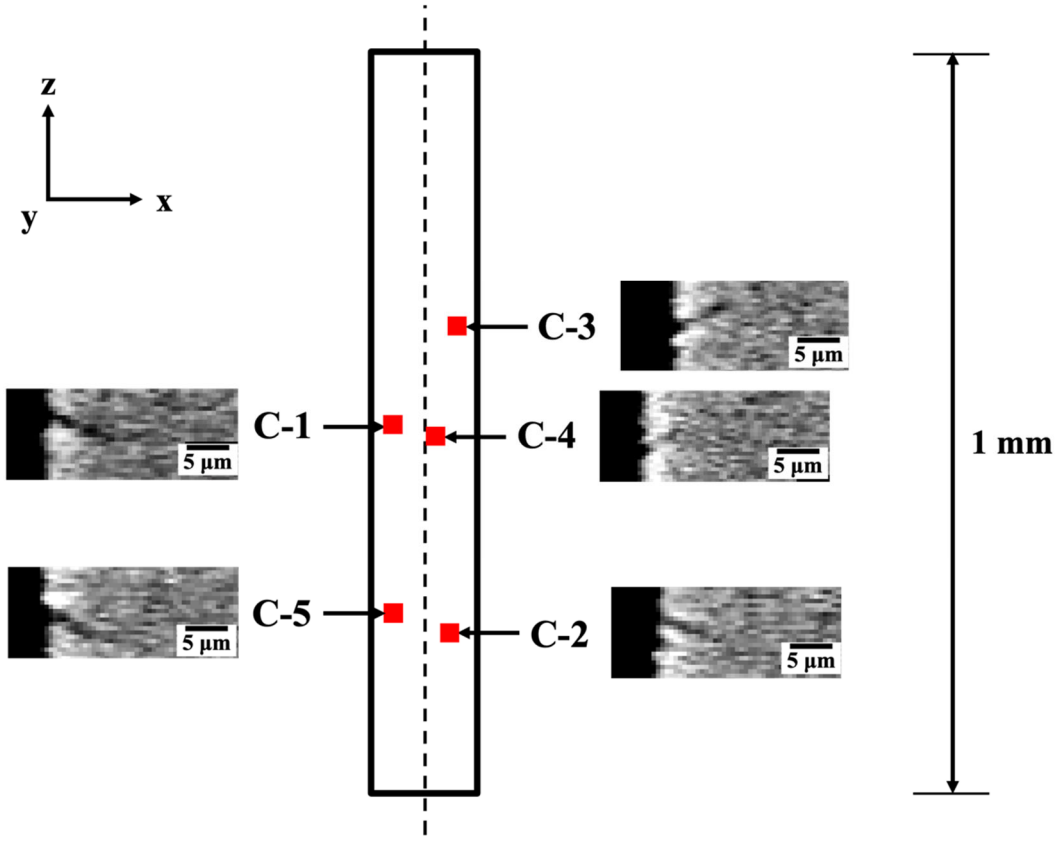

(b) Crack-initiation location on the side-view of the specimen and the images of the cracks initiated on the virtual cross section parallel to the longitudinal direction

Fig. 6 Crack-initiation status.

3.2 Crack-propagation process

As an example, the propagation process of C-1 until 7000 cycles is depicted in Fig. 7, which shows the micro-CT images projected on a plane perpendicular to the loading axis. The crack depths and lengths (b and $2a$, respectively) were measured from these images. In the CT images, the low-density materials or the defects and voids appear darker than their surroundings. Therefore, the shadow features in Fig. 7 indicate an open crack. After the crack is initiated, it propagates symmetrically from the center. The relationship between the crack length, $2a$, and number of cycles, N, for all five cracks is demonstrated in Fig. 8. The fatigue life of this specimen was 9751 cycles, and C-1 was the main crack that led to the final fracture.

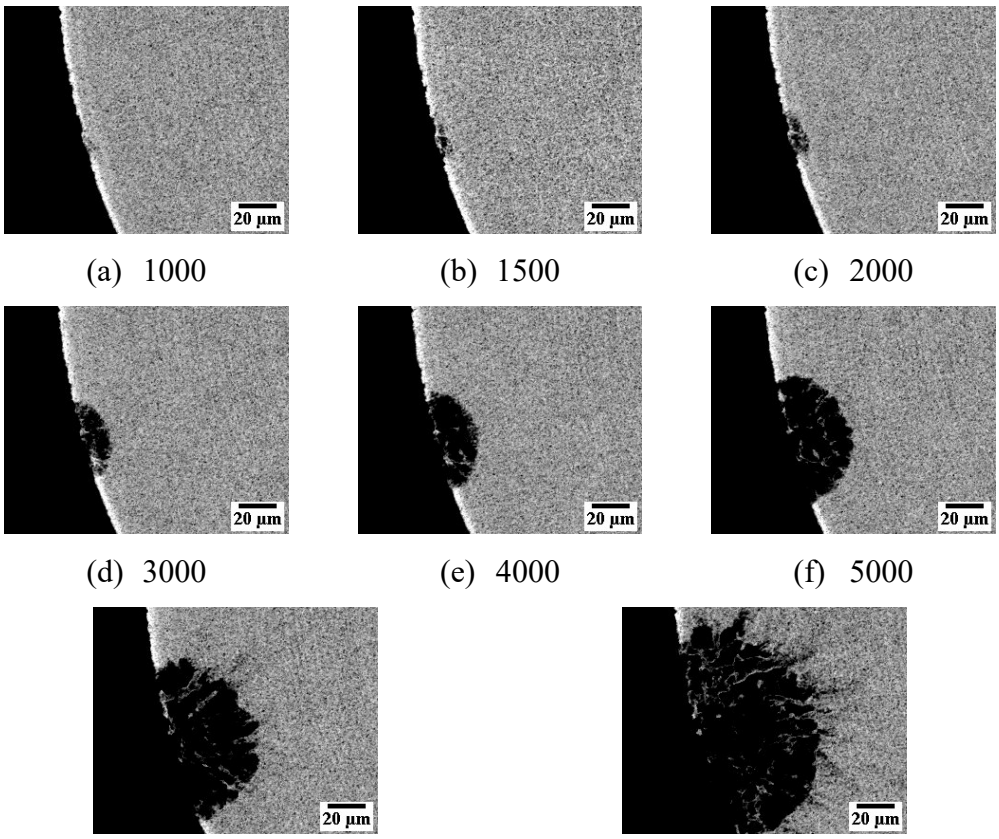

Fig. 7 Propagation process of crack C-1: Micro-CT images projected on a plane perpendicular to the loading axis.

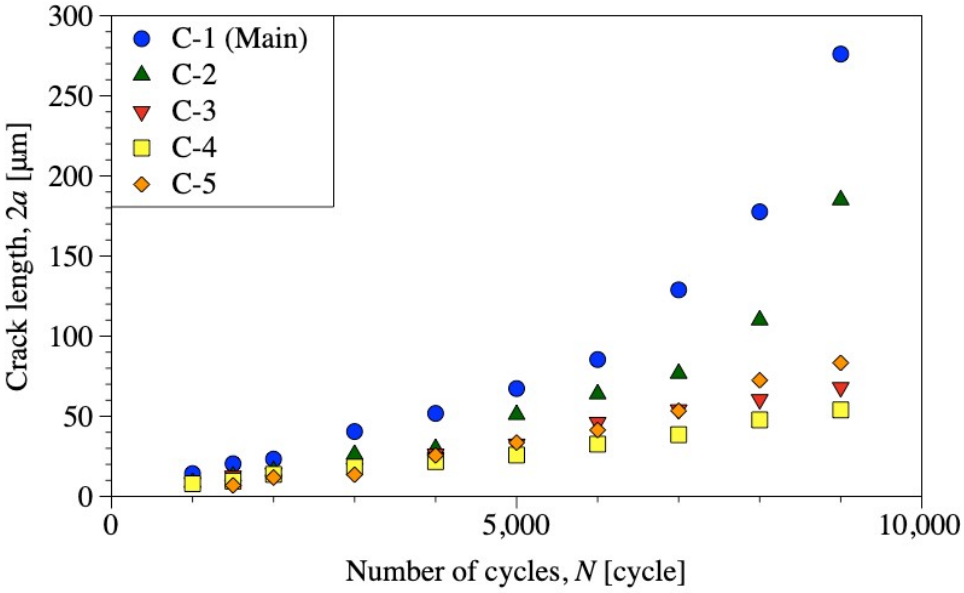

Fig. 8 Relationship between the crack length and number of cycles.

3.2.1 Crack-shape evolution and the corresponding stress intensity factor

According to Fig. 7, crack C-1 exhibits a semi-elliptic shape before 4000 cycles (Fig. 7 (a)–(e)), and changes into a semicircular shape after 5000 cycles (Fig. 7 (f)–(h)). To describe the crack shape, the aspect ratio of the crack (b/a) was plotted with respect to the crack length, as shown in Fig. 9. In general, the deviation in b/a of all five cracks is relatively large in the small crack-length region. However, when the crack length increases, the deviation in b/a becomes less pronounced, and the value of b/a approaches 1. This indicates that microstructural factors affect the propagation of a small crack, which leads to a less stable crack shape than a large crack.

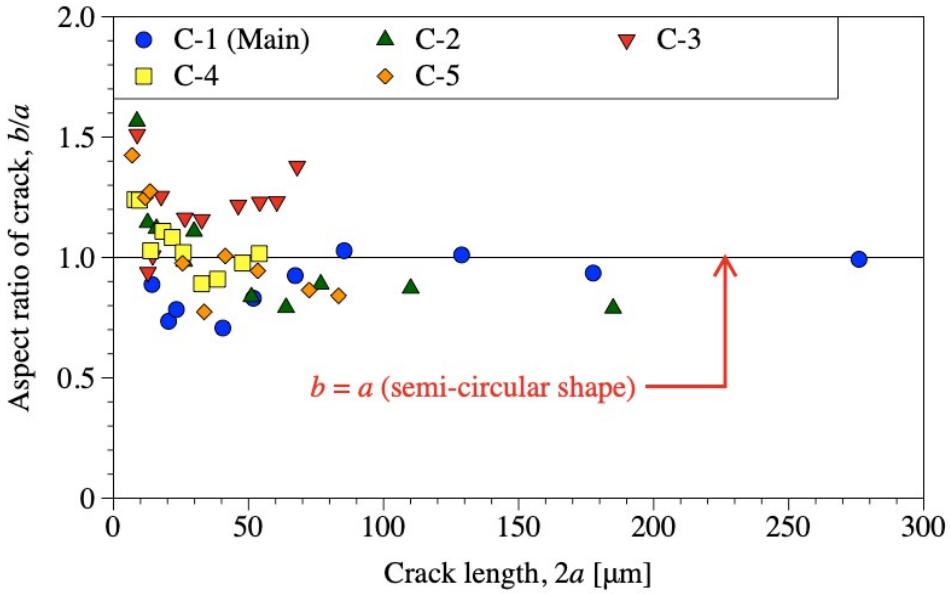

Fig. 9 Relationship between the aspect ratio of the crack, b/a, and crack length, $2a$.

For comparison with the large cracks, we adopted the stress intensity factor range, ΔK, for the small cracks. To calculate ΔK corresponding to the current crack shape, we have used the method proposed by Nisitani et al. [37], as shown in Eq. (1):

$$\Delta K = F_1 \Delta\sigma\sqrt{\pi b}, \tag{1}$$

where ΔK is the stress intensity factor range at the crack front; F_1 represents a factor related to the aspect ratio in terms of the crack geometry, b/a, and the ratio of the crack depth to the specimen radius, b/r. Some F_1 values are listed in Table 3. The calculated

values were linearly interpolated according to the crack length and shape. $\Delta\sigma$ indicates the range of applied positive stress.

Table 3 F_1 values in terms of the crack geometry, b/a, and the ratio of the crack depth to the specimen radius, b/r [37].

b/r / *b/a*	0	0.125	0.250	0.375	0.5
1	0.66	0.665	0.683	0.714	0.758
0.5	0.884	0.890	0.980	0.976	1.064

3.2.2 Crack propagation rate

A comparison between the da/dN values of all five cracks against ΔK is presented in Fig. 10. The crack lengths and shapes of these five cracks are dissimilar, as shown in Fig. 8 and Fig. 9; however, their da/dN-ΔK curves exhibit a good agreement, signifying that the shape evolution of naturally initiated cracks does not critically affect the da/dN–ΔK curves. In addition, with a decrease in ΔK, the deviation in da/dN increases. Tokaji et al. also conducted a ΔK-decreasing test using a compact tension specimen of Ti–22V–4Al, represented by the dashed line in Fig. 10 [9]. In the high-ΔK regime (over 4–5 MPa√m), the da/dN–ΔK in the present study was consistent with that of large cracks. In contrast, in the low-ΔK regime, most of da/dN of small cracks were faster than that of large cracks at the same ΔK. The above results can be explained by the fact that a smaller crack follows a path with less resistance, and its growth can be hindered by the local microstructural factors.

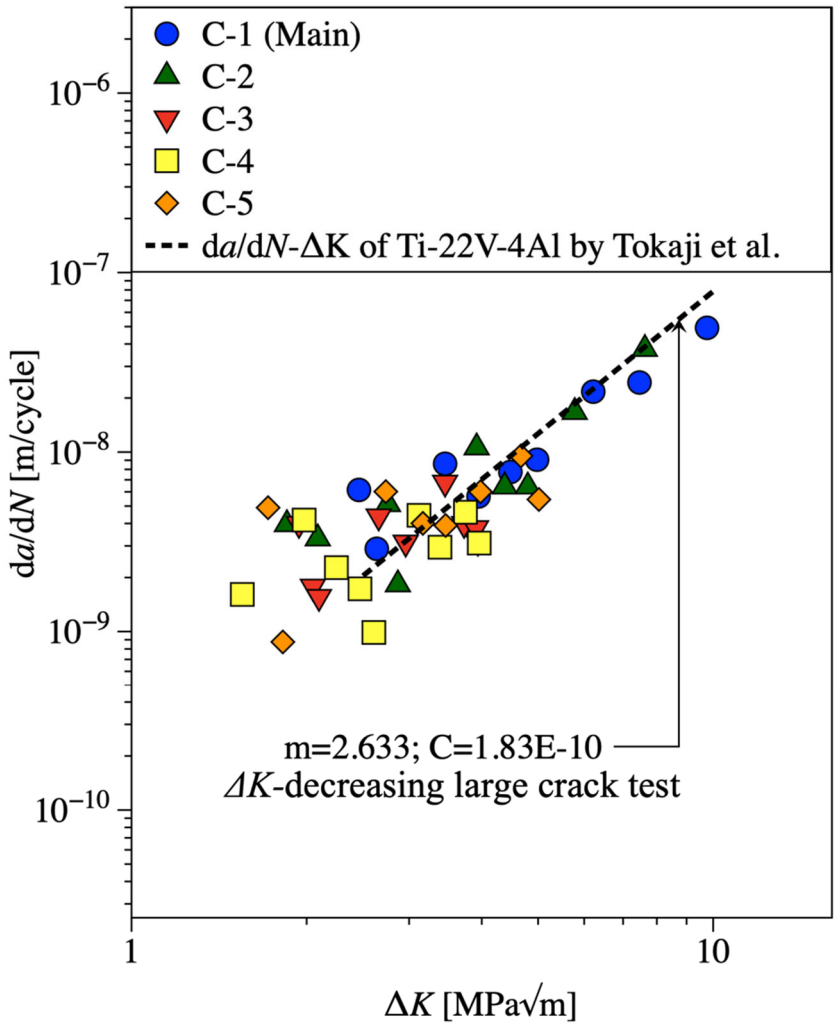

Fig. 10 Relationship between the crack propagation rate and the stress intensity factor range.

3.3 Crack-initiation process

The five cracks initiated naturally but at different cycles. Yoshinaka et al. defined the crack initiation rate, $(\frac{\mathrm{d}a}{\mathrm{d}N}\Big|_{\mathrm{i}})$, as shown in Eq. (2), which is comparable to the crack propagation rate but describes the speed of crack initiation [38].

$$\left.\frac{\mathrm{d}a}{\mathrm{d}N}\right|_{i} = \frac{a_{\mathrm{ini}}}{N_{\mathrm{i}} - N_{\mathrm{i-1}}} \tag{2}$$

Here, a_{ini} is half of the initial crack length, N_{i} is the number of cycles corresponding to

the detection of the first crack (crack initiation life), and N_{i-1} is the number of cycles one step before N_i during the CT scanning. Because of the consistent scanning intervals at the early stage of the experiment, $N_i - N_{i-1}$ was 500 for all five cracks, thus eliminating the influence of dissimilar crack initiation lives. The initiation rate of all five cracks against ΔK are illustrated in Fig. 11, along with the integration of the crack propagation rate shown in Fig. 10 for comparison. The crack initiation rate was plotted at approximately 10^{-8} m/cycles, which is 5 to 10 times larger than the crack propagation rate in the early stage. Meanwhile, the crack initiation rate has a more concentrated distribution than the crack propagation rate. Therefore, the crack initiation process has a consistent mechanism regardless of the number of cracks and occurs faster than the subsequent propagation process. In a previous study, we pointed out that the cracks in beta titanium alloys are initiated by slippage in a grain [11], which further implies that the rapid crack-initiation process is due to the low crack-growth resistance in a grain with a favorable slip-system orientation. Other studies on the crack-initiation process also infer similar results. Yoshinaka et al. reported that the internal crack initiation rate in Ti–6Al–4V is similar among various cracks and faster than the subsequent propagation rate [38]. Meanwhile, in an alpha titanium alloy, Pilchak et al. discovered that the crack initiated on the alpha grain facet in the faceted growth mode is one or two orders of magnitude faster than that in the striated growth mode [39].

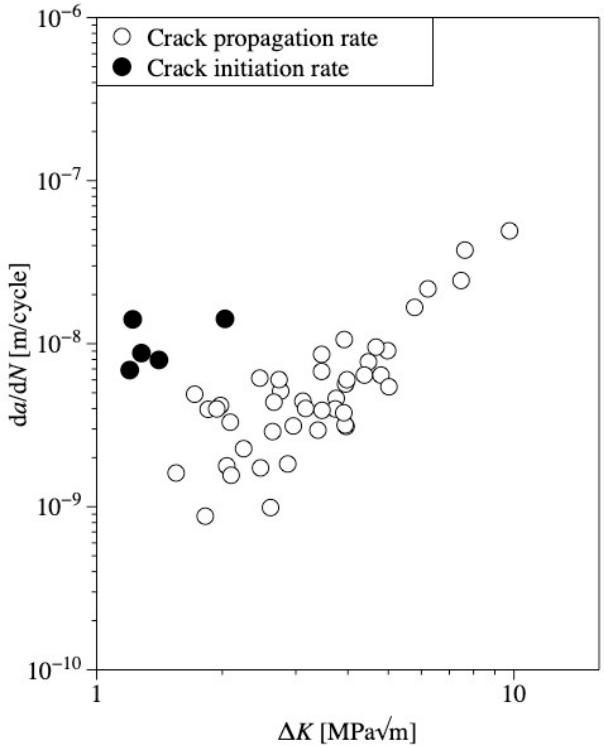

Fig. 11 Relationship between the crack initiation rate and the stress intensity factor range.

4. Nano-CT results

4.1 Optimization of the test conditions for microstructural visualization

Microstructural visualization by nano-CT is sensitive to many parameters, such as the specimen diameter, material chemical composition, X-ray energy, and imaging exposure time, and qualitative discussions of these parameters are complicated. In this section, the results of experiments conducted for optimizing the nano-CT-imaging conditions are presented. The FOV of all subsequent nano-CT images is approximately 60 μm × 60 μm.

In general, increasing the exposure time and decreasing the X-ray energy are often considered as simple, useful techniques to improve the image quality using existing X-ray equipment. In particular, the latter is effective from the viewpoint of increasing the X-ray absorption coefficient and its sensitivity between different phases in a material. The nano-CT images of the exact location of the specimen at the exposure times of 1000 ms and 4000 ms are illustrated in Fig. 12 (a) and Fig. 12 (b), respectively. The specimen had a diameter of 0.7 mm and was imaged under 30 keV; its corresponding

transmittance was approximately 18%. The grain boundary was barely observed at an exposure time of 1000 ms. In contrast, the grain boundary and acicular alpha-phase precipitation are discernible at 4000 ms of exposure. In addition, we attempted to apply a lower X-ray energy (20 keV) using a thinner specimen with 0.2 mm diameter. In this case, the corresponding transmittance was 21%, which is similar to the results mentioned previously. The 20 keV nano-CT image presented in Fig. 13 was obtained under an exposure time of 1000 ms (same as that in Fig. 12 (a)). The microstructural details, such as grain boundary, acicular alpha-phase precipitation, and residual beta-phase, are more clearly observed in Fig. 13 than in Fig. 12 (a) and Fig. 12 (b), indicating that the decrease in X-ray energy significantly improves the quality of microstructural visualization. However, conducting fatigue tests with a specimen of 0.2 mm diameter is challenging and may not attract industrial attention. Therefore, we adopted the second-best condition of Fig. 12 (b) using a specimen of 0.7 mm diameter with 30 keV X-ray energy and 4000 ms exposure time.

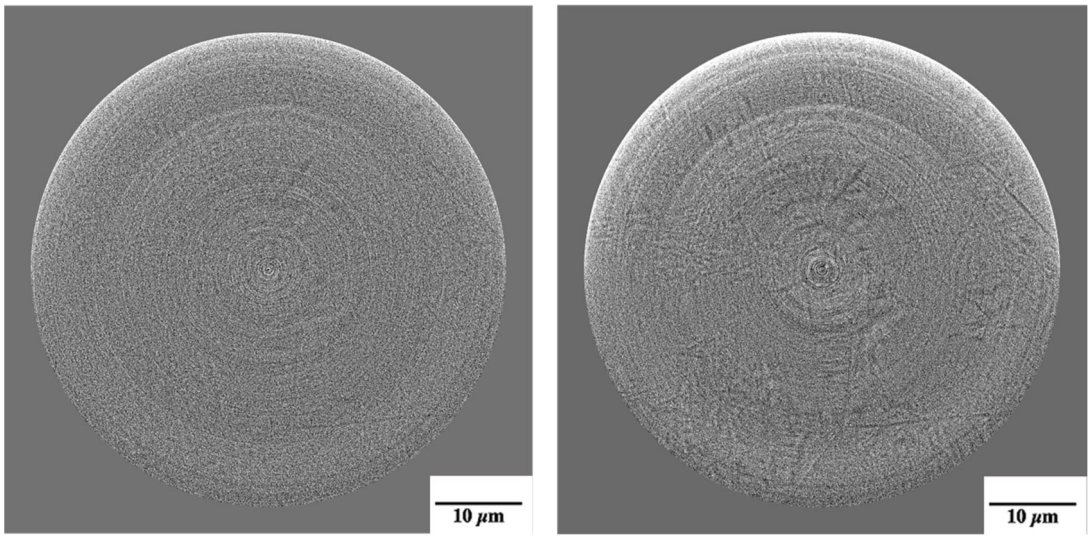

(a) Exposure time: 1000 ms (b) Exposure time: 4000 ms

Fig. 12 Nano-CT-imaging conditions in terms of the exposure time (specimen diameter: 0.7 mm; X-ray energy: 30 keV; transmittance: ~18%).

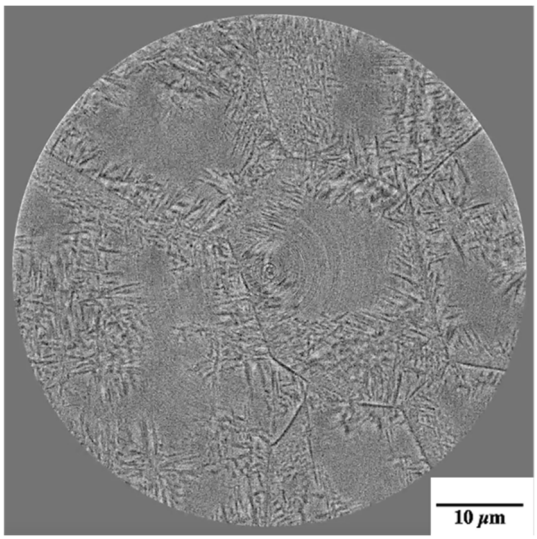

Fig. 13 Nano-CT-imaging conditions in terms of the X-ray energy (specimen diameter: 0.2 mm; X-ray energy: 20 keV; transmittance: ~21%, exposure time: 1000 ms).

4.2 Crack initiation site in the microstructure

The crack initiation site in the microstructure of beta titanium alloys is much debated. Tokaji et al. mentioned that the crack presumably initiates from the alpha phase or the grain boundary in Ti–22V–4Al [40]. Uematsu et al. pointed out that cracks initiate in the beta grain with rich alpha-phase precipitation in Ti–22V–4Al [41]. Shiozawa et al. reported that the crack originates inside a beta grain in Ti–15V–3Cr–3Sn–3Al (Ti-15-3-3-3) [42]. Therefore, we focused on revealing the mutual relationship between the crack initiation site and microstructure using nano-CT.

The 3D morphology of crack C-1 at 1500 cycles is shown in Fig. 14, and the sliced images are presented in Fig. 15. The grain boundary and acicular alpha phase are discernible from Fig. 15 (a) and (b), which are the nano-CT images resliced in the directions of crack length and depth, respectively. First, the crack does not cross the grain boundary in either image, which indicates that the crack initiates inside the beta grain rather than the grain boundary. In addition, the crack is located at the center of the grain. As mentioned in Section 3.2, the crack propagates symmetrically, which implies that the crack presumably initiates from the center and not near any side of the grain boundary. Although it is difficult to recognize the acicular alpha-phase precipitation near the crack, the comparison of the microstructure and nano-CT images in Fig. 1 and

Fig. 13, respectively, reveals that the grain center mostly has a residual beta phase. These results indicate that the crack likely initiates from a residual β phase without alpha-phase precipitation. Lütjering et al. reported that fracture deformation in high-strength Al and Ti alloys preferentially occurs at the grain boundary owing to the soft precipitation-free zones (PFZs) lacking solute atoms [43]. Although this conclusion is inconsistent with our findings, the PFZ theories support the findings of this study. This is because the PFZs in our material also exist in the center of the grain owing to the incomplete alpha-phase precipitation process from aging. Therefore, the PFZs at both the grain boundary and the grain center can deform; the crack is initiated at either of these locations.

The nano-CT image projected on a plane perpendicular to the loading axis is shown in Fig. 15 (c). Similar to that observed in the micro-CT images in Fig. 7, an open crack is reflected by the shadow feature. The crack propagation is restrained by the grain boundary, as indicated by the red arrow. This phenomenon is referred to as the grain boundary blocking effect, which occurs when the crack size is similar to or below the grain size order [44–46]. Therefore, we can conclude that, at the early stage of a crack, its facet-like behavior and boundary blocking effect can be captured by nano-CT.

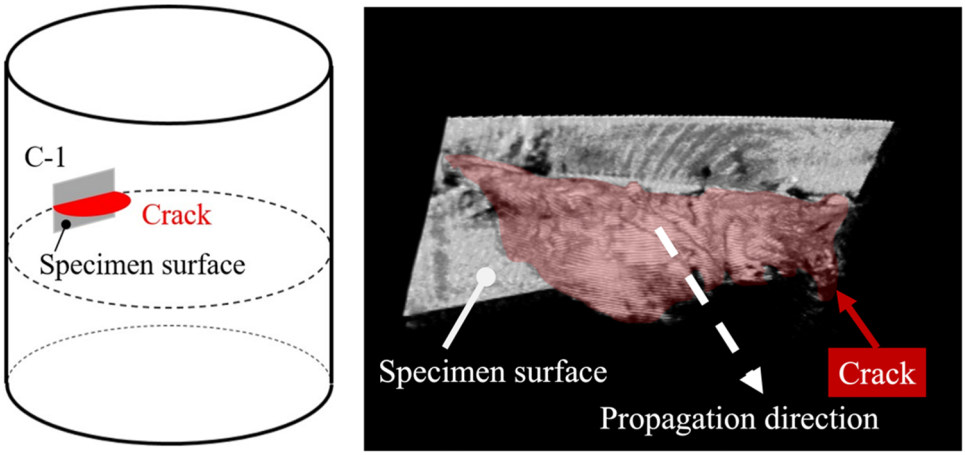

Fig. 14 3D morphology of C-1 at 1500 cycles by nano-CT.

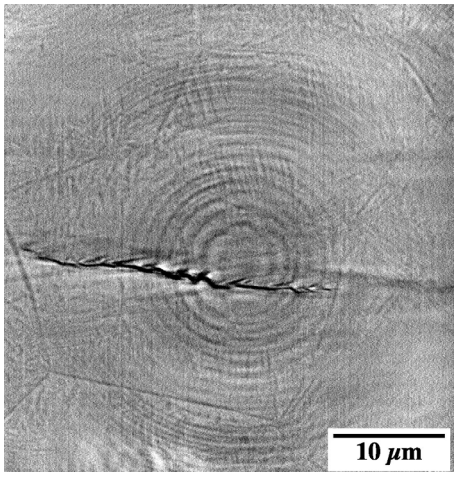

(a) Longitudinal section
(parallel to crack length direction)

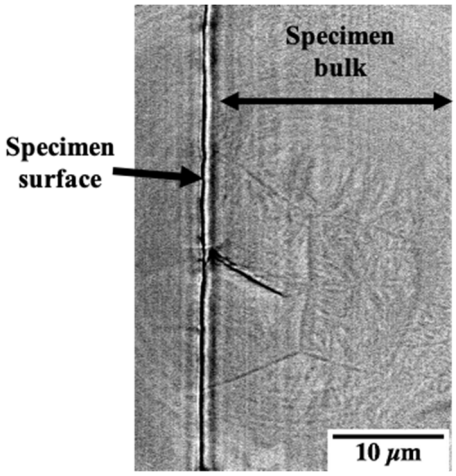

(b) Longitudinal section
(parallel to crack depth direction)

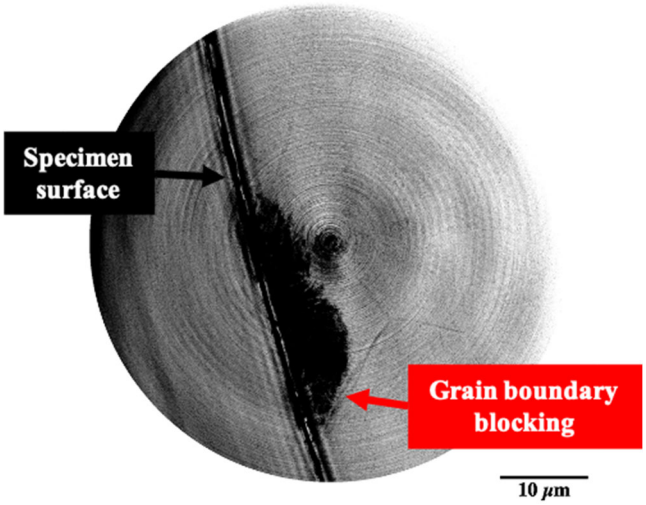

(c) Crack projected on a plane
perpendicular to the loading axis

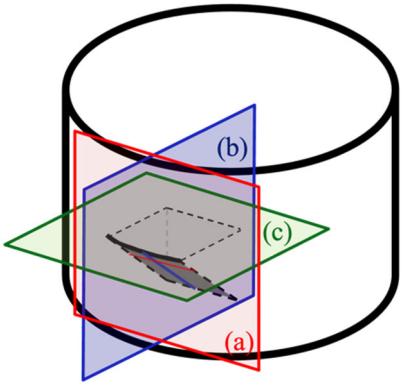

(d) Schematic of sectioning
and projection view

Fig. 15 Nano-CT images of main crack C-1 at 1500 cycles.

5. Conclusions

This paper presents an investigation of small crack initiation and propagation behavior observed by multiscale X-ray tomography involving micro-CT and nano-CT. The following conclusions were obtained:

1. Crack initiation and propagation were investigated by micro-CT. Multiple cracks were initiated at the 1000th and 1500th cycles, equivalent to approximately 10% of the fatigue life (fractured at 9751 cycles). The average crack-initiation length was 9.3 μm, which was much smaller than that of the grain size.

2. The main crack propagated with a semi-elliptic shape until 4000 cycles and subsequently evolved into a semicircular shape. Similarly, other subcracks also exhibited an unstable crack-shape behavior at the early stage but approached a semicircular shape during their propagation.

3. The propagation rates of the five detected cracks illustrated a good agreement with the da/dN–ΔK curve, indicating that the crack-shape evolution was negligibly related to da/dN–ΔK. Moreover, with the decrease in ΔK, the deviation in the crack propagation rate increased. On the other hand, the crack initiation rate exhibited lesser deviation and was larger than the crack propagation rate, which can be explained by the uniform crack-initiation mechanism and the relatively low crack-growth resistance in the beta grain.

4. Both the microstructural details of the beta titanium alloy and the mutual interactions between the crack and its surrounding microstructure were clearly recognized by nano-CT. The crack was initiated inside the beta grain, which lacked alpha-phase precipitation. In addition, the grain boundary blocking effect could also be captured.

5. According to the results of nano-CT, the microstructural effect can account for the phenomenon mentioned in conclusions 2 and 3, thereby evincing that the microstructural effect plays a significant role in the small-crack behavior in beta titanium alloys.

Acknowledgments: We would like to express our sincere gratitude to Daido Steel Co., Ltd. for providing the experimental material. The synchrotron radiation experiments were performed at BL20XU, SPring-8 (proposal nos. 2020A0172) with the approval of the Japan Synchrotron Radiation Research Institute (JASRI). This research was supported by the f3 Engineering Education and Research Center at the Faculty of Engineering, Hokkaido University, and an Ambitious Doctoral Fellowship from Hokkaido University. We are grateful to Anna Ohkawara for her technical support during the experiments.

Funding: This research was funded by the Japan Society for the Promotion of Science, Japan (grant number: Scientific Research (A, 18H03748 and 21H04529)).

References:

[1] Kolli RP, Devaraj A. A review of metastable beta titanium alloys. Metals (Basel) 2018;8. https://doi.org/10.3390/met8070506.

[2] Cotton JD, Briggs RD, Boyer RR, Tamirisakandala S, Russo P, Shchetnikov N, et al. State of the Art in Beta Titanium Alloys for Airframe Applications. JOM 2015;67:1281–303. https://doi.org/10.1007/s11837-015-1442-4.

[3] Boyer RR, Briggs RD. The use of β titanium alloys in the aerospace industry. J Mater Eng Perform 2005;14:681–5. https://doi.org/10.1361/105994905X75448.

[4] Jha SK, Ravichandran KS. High-cycle fatigue resistance in beta-titanium alloys. Jom 2000;52:30–5. https://doi.org/10.1007/s11837-000-0097-x.

[5] Qiu J, Feng X, Ma Y, Lei J, Liu Y, Huang A, et al. Fatigue crack growth behavior of beta-annealed Ti-6Al-2Sn-4Zr-xMo (x = 2, 4 and 6) alloys: Influence of microstructure and stress ratio. Int J Fatigue 2016;83:150–60. https://doi.org/10.1016/j.ijfatigue.2015.10.009.

[6] Kocan M, Rack HJ, Wagner L. Fatigue performance of metastable β titanium alloys: Effects of microstructure and surface finish. J. Mater. Eng. Perform., vol. 14, Springer; 2005, p. 765–72. https://doi.org/10.1361/105994905X75583.

[7] Tokaji K, Kariya H. Mean stress dependence of fatigue strength and subsurface crack initiation in Ti-15Mo-5Zr-3Al alloy. Mater Sci Eng A 2000;281:268–74. https://doi.org/10.1016/S0921-5093(99)00710-8.

[8] Huang C, Zhao Y, Xin S, Tan C, Zhou W, Li Q, et al. Effect of microstructure on high cycle fatigue behavior of Ti–5Al–5Mo–5V–3Cr–1Zr titanium alloy. Int J Fatigue 2017;94:30–40. https://doi.org/10.1016/j.ijfatigue.2016.09.005.

[9] Tokaji K, Takafuji S, Ohya K, Kato Y, Mori K. Fatigue behaviour of beta Ti-22V-4Al alloy subjected to surface-microstructural modification. J Mater Sci 2003;38:1153–9. https://doi.org/10.1023/A:1022880914473.

[10] Campanelli LC, da Silva PSCP, Bolfarini C. High cycle fatigue and fracture behavior of Ti-5Al-5Mo-5V-3Cr alloy with BASCA and double aging treatments. Mater Sci Eng A 2016;658:203–9. https://doi.org/10.1016/j.msea.2016.02.004.

[11] Xue G, Nakamura T, Fujimura N, Takahashi K, Oguma H. Initiation and Propagation Processes of Internal Fatigue Cracks in β Titanium Alloy Based on Fractographic Analysis. Appl Sci 2020;11:131. https://doi.org/10.3390/app11010131.

[12] Benedetti M, Fontanari V, Lütjering G, Albrecht J. The effect of notch plasticity on the behaviour of fatigue cracks emanating from edge-notches in high-strength β-titanium alloys. Eng Fract Mech 2008;75:169–87. https://doi.org/10.1016/j.engfracmech.2007.03.037.

[13] Cox BN. Inductions from Monte Carlo simulations of small fatigue cracks. Eng Fract Mech 1989;33:655–70. https://doi.org/10.1016/0013-7944(89)90048-9.

[14] Ritchie RO, Peters JO. Small fatigue cracks: Mechanics, mechanisms and engineering applications. Mater Trans 2001;42:58–67. https://doi.org/10.2320/matertrans.42.58.

[15] Kruzic JJ, Campbell JP, Ritchie RO. On the fatigue behavior of γ-based titanium aluminides: Role of small cracks. Acta Mater 1999;47:801–16. https://doi.org/10.1016/S1359-6454(98)00409-1.

[16] Hu YN, Wu SC, Withers PJ, Zhang J, Bao HYX, Fu YN, et al. The effect of manufacturing defects on the fatigue life of selective laser melted Ti-6Al-4V structures. Mater Des 2020;192:108708. https://doi.org/10.1016/j.matdes.2020.108708.

[17] Wu Z, Wu S, Bao J, Qian W, Karabal S, Sun W, et al. The effect of defect population on the anisotropic fatigue resistance of AlSi10Mg alloy fabricated by laser powder bed fusion. Int J Fatigue 2021;151:106317. https://doi.org/10.1016/j.ijfatigue.2021.106317.

[18] Nakayama T, Yuse F, Tsubokawa Y, Matsui J. Direct observations of cracks and voids in structural materials by X-ray imaging using ultra-bright synchrotron radiation. ISIJ Int 2003;43:589–96. https://doi.org/10.2355/isijinternational.43.589.

[19] Wu S, Xiao T, Withers PJ. The imaging of failure in structural materials by synchrotron radiation X-ray microtomography. Eng Fract Mech 2017;182:127–

56. https://doi.org/10.1016/j.engfracmech.2017.07.027.

[20] Qian W, Wu S, Wu Z, Ahmed S, Zhang W, Qian G, et al. In situ X-ray imaging of fatigue crack growth from multiple defects in additively manufactured AlSi10Mg alloy. Int J Fatigue 2022;155:106616. https://doi.org/10.1016/J.IJFATIGUE.2021.106616.

[21] Toda H, Takijiri A, Azuma M, Yabu S, Hayashi K, Seo D, et al. Damage micromechanisms in dual-phase steel investigated with combined phase- and absorption-contrast tomography. Acta Mater 2017;126:401–12. https://doi.org/10.1016/j.actamat.2017.01.010.

[22] Birosca S, Buffiere JY, Karadge M, Preuss M. 3-D observations of short fatigue crack interaction with lamellar and duplex microstructures in a two-phase titanium alloy. Acta Mater 2011;59:1510–22. https://doi.org/10.1016/j.actamat.2010.11.015.

[23] Babout L, Jopek Ł, Preuss M. 3D characterization of trans- and inter-lamellar fatigue crack in (α + β) Ti alloy. Mater Charact 2014;98:130–9. https://doi.org/10.1016/j.matchar.2014.10.017.

[24] Chapman TP, Kareh KM, Knop M, Connolley T, Lee PD, Azeem MA, et al. Characterisation of short fatigue cracks in titanium alloy IMI 834 using X-ray microtomography. Acta Mater 2015;99:49–62. https://doi.org/10.1016/j.actamat.2015.07.069.

[25] Messager A, Junet A, Palin-Luc T, Buffiere JY, Saintier N, Ranc N, et al. In situ synchrotron ultrasonic fatigue testing device for 3D characterisation of internal crack initiation and growth. Fatigue Fract Eng Mater Struct 2020;43:558–67. https://doi.org/10.1111/ffe.13140.

[26] Yoshinaka F, Nakamura T, Takeuchi A, Uesugi M, Uesugi K. Initiation and growth behaviour of small internal fatigue cracks in Ti-6Al-4V via synchrotron radiation microcomputed tomography. Fatigue Fract Eng Mater Struct 2019;42:2093–105. https://doi.org/10.1111/ffe.13085.

[27] King A, Ludwig W, Herbig M, Buffire JY, Khan AA, Stevens N, et al. Three-dimensional in situ observations of short fatigue crack growth in magnesium.

Acta Mater 2011;59:6761–71. https://doi.org/10.1016/j.actamat.2011.07.034.

[28] Herbig M, King A, Reischig P, Proudhon H, Lauridsen EM, Marrow J, et al. 3-D growth of a short fatigue crack within a polycrystalline microstructure studied using combined diffraction and phase-contrast X-ray tomography. Acta Mater 2011;59:590–601. https://doi.org/10.1016/j.actamat.2010.09.063.

[29] Zhang H, Toda H, Hara H, Kobayashi M, Kobayashi T, Sugiyama D, et al. Three-dimensional visualization of the interaction between fatigue crack and micropores in an aluminum alloy using synchrotron X-ray microtomography. Metall Mater Trans A Phys Metall Mater Sci 2007;38:1774–85. https://doi.org/10.1007/s11661-007-9214-6.

[30] Takeuchi A, Suzuki Y. Recent progress in synchrotron radiation 3D-4D nano-imaging based on X-ray full-field microscopy. Microscopy 2020;69:259–79. https://doi.org/10.1093/jmicro/dfaa022.

[31] Takeuchi A, Uesugi K, Uesugi M, Toda H, Hirayama K, Shimizu K, et al. High-energy X-ray nanotomography introducing an apodization Fresnel zone plate objective lens. Rev Sci Instrum 2021;92:023701. https://doi.org/10.1063/5.0020293.

[32] Suzuki Y, Uesugi K, Takimoto N, Fukui T, Aoyama K, Takeuchi A, et al. Construction and commissioning of A 248 m-long beamline with X-ray undulator light source. AIP Conf. Proc., vol. 705, American Institute of PhysicsAIP; 2004, p. 344–7. https://doi.org/10.1063/1.1757804.

[33] Takeuchi A, Uesugi K, Uesugi M, Yoshinaka F, Nakamura T. Nondestructive multiscale X-Ray tomography by combining microtomography and high-energy phase-contrast nanotomography. Microsc Microanal 2018;24:108–9. https://doi.org/10.1017/s1431927618012928.

[34] Daido Steel Co., Ltd. DAT51 (High Strength β-Titanium Alloy) with Improved Press Workability. n.d. https://www.daido.co.jp/en/products/titanium/strength/index.html (accessed December 19, 2020).

[35] Takanashi K, Kashima S, Yoshinaka F, Nakamura T, Fujimura N, Takahashi

K. Fatigue crack initiation and propagation properties of Ti-22V-4Al. Proc Mater Mech Conf 2017;2017:PS29. https://doi.org/10.1299/jsmemm.2017.ps29.

[36] Schneider CA, Rasband WS, Eliceiri KW. NIH Image to ImageJ: 25 years of image analysis. Nat Methods 2012;9:671–5. https://doi.org/10.1038/nmeth.2089.

[37] Nisitani H, Chen DH. Stress Intensity Factor for a Semi-Elliptic Surface Crack in a Shaft under Tension. Trans Japan Soc Mech Eng Ser A 1984;50:1077–82. https://doi.org/10.1299/kikaia.50.1077.

[38] Yoshinaka F, Nakamura T, Takaku K, Sshiozawa D, Nakai Y, Uesugi K. Observation of the initial process of internal fracture in very high cycle fatigue in Ti-6Al-4V by synchrotron radiation μCT imaging. Trans JSME (in Japanese) 2017;83:1–15. https://doi.org/10.1299/transjsme.17-00104.

[39] Pilchak AL. Fatigue crack growth rates in alpha titanium: Faceted vs. striation growth. Scr Mater 2013;68:277–80. https://doi.org/10.1016/J.SCRIPTAMAT.2012.10.041.

[40] Tokaji K, Ohya K, Kariya H. Subsurface fatigue crack initiation in beta titanium alloys. Fatigue Fract Eng Mater Struct 2000;23:759–66. https://doi.org/10.1046/j.1460-2695.2000.00325.x.

[41] Uematsu Y, Kakiuchi T, Hattori K. EBSD-assisted fractography of sub-surface fatigue crack initiation mechanism in the ultrasonic-shot-peened βeta-type titanium alloy. Fatigue Fract Eng Mater Struct 2018;41:2239–48. https://doi.org/10.1111/ffe.12812.

[42] Shiozawa K, Kuroda Y, Nishino S. Effect of stress ratio on subsurface fatigue crack initiation behavior of beta-type titanium alloy. Nihon Kikai Gakkai Ronbunshu, A Hen/Transactions Japan Soc Mech Eng Part A 1998;64:2528–35. https://doi.org/10.1299/kikaia.64.2528.

[43] Lütjering G, Albrecht J, Sauer C, Krull T. The influence of soft, precipitate-free zones at grain boundaries in Ti and Al alloys on their fatigue and fracture behavior. Mater Sci Eng A 2007;468–470:201–9.

https://doi.org/10.1016/j.msea.2006.07.168.

[44] Tanaka K, Akiniwa Y, Nakai Y, Wei RP. Modelling of small fatigue crack growth interacting with grain boundary. Eng Fract Mech 1986;24:803–19. https://doi.org/10.1016/0013-7944(86)90266-3.

[45] Zhai T, Wilkinson AJ, Martin JW. Crystallographic mechanism for fatigue crack propagation through grain boundaries. Acta Mater 2000;48:4917–27. https://doi.org/10.1016/S1359-6454(00)00214-7.

[46] Lankford J. The Growth of Small Fatigue Cracks in 7075–T6 Aluminum. Fatigue Fract Eng Mater Struct 1982;5:233–48. https://doi.org/10.1111/j.1460-2695.1982.tb01251.x.